

# Iterative Image Restoration Combining Total Variation Minimization and a Second-Order Functional\*

Marius Lysaker<sup>†</sup>      Xue-Cheng Tai<sup>‡</sup>

## Abstract

A noise removal technique using partial differential equations (PDEs) is proposed here. It combines the Total Variational (TV) filter with a fourth-order PDE filter. The combined technique is able to preserve edges and at the same time avoid the staircase effect in smooth regions. A weighting function is used in an iterative way to combine the solutions of the TV-filter and the fourth-order filter. Numerical experiments confirm that the new method is able to use less restrictive time step than the fourth-order filter. Numerical examples using images with objects consisting of edge, flat and intermediate regions illustrate advantages of the proposed model.

**Key words.** Iterative image restoration, convex combination, characteristic features, PDEs.

## 1 Introduction

An approach to recover an image  $u$  from a noisy observation  $u_0$  is proposed in this work. Digital images can basically be decomposed into three distinguished areas; flat regions, regions with a smooth change in the intensity value, and jumps. The aim of all noise removal algorithms is to restore and enhance these characteristics by filtering out noise. Total Variation (TV) minimization is a successful approach to recover images with sharp edges. This method was proposed by Rudin, Osher

---

\*This work has been supported by the Research Council of Norway.

<sup>†</sup>M. Lysaker is with the Department of Scientific Computing, Simula Research Laboratory AS, Norway (email: mariul@simula.no).

<sup>‡</sup>X.-C. Tai is with the Department of Mathematics, University of Bergen, N-5008, Bergen, Norway (tai@mi.uib.no).

and Fatemi (ROF) in [1]. The TV minimization method finds  $u$  where the following is satisfied

$$\min_u E_1(u), \quad \text{where } E_1(u) = \int_{\Omega} |\nabla u| \, dxdy + \frac{\lambda_1}{2} \int_{\Omega} |u - u_0|^2 \, dxdy. \quad (1)$$

Here,  $\Omega \subset \mathbb{R}^2$  is the domain where the image is defined,  $\lambda_1 > 0$  is a parameter that controls contribution of the fidelity term  $\int_{\Omega} |u - u_0|^2 \, dxdy$ , and  $\int_{\Omega} |\nabla u| \, dxdy$  is in fact the total variation of  $u$ ; see Ziemer [2] and Giusti [3] for definitions. When  $u$  is not differentiable,  $|\nabla u|$  is understood as a measure. More precisely,

$$\int_{\Omega} |\nabla u| \, dxdy = \sup \left\{ \int_{\Omega} u \operatorname{div} v \, dxdy : v = (v_1, v_2) \in C_0^{\infty}(\Omega), \right. \\ \left. v_1^2(x, y) + v_2^2(x, y) \leq 1 \text{ for } (x, y) \in \Omega \right\}. \quad (2)$$

See p. 221 of [2] for some more details. This term is generally called a regularization term and it is used here to penalize oscillations. A superior advantage of the TV-norm regularization is that discontinuities are allowed. However, both from a theoretical [4, 5] and experimental [6, 7, 8] point of view, it has been shown that the TV-norm transforms smooth signal into piecewise constants, the so-called staircase effect. To overcome this spurious effect, higher-order PDEs have been of special interest over the last few years [6, 8, 9, 10, 11, 12, 13, 14, 15, 16]. The theoretical analysis of [13, 14, 15] reveals that fourth-order PDEs enjoy some special properties that are not valid for the second-order PDEs. The higher-order PDEs are generally coming from the minimization of functionals as

$$\min_u \int_{\Omega} F(x_1, x_2, \dots, x_k, u, du, d^2u, \dots, d^k u) \, dx_1 dx_2 \dots dx_k, \quad (3)$$

where  $d^k u$  is the partial derivatives of  $u$  of order  $k$ . For  $\Omega \subset \mathbb{R}^n$  and  $n \geq 2$ , mixed derivative may occur in (3). One of the functionals of focus in this paper was first proposed by Lysaker, Lundervold and Tai (LLT) in a previous work [6]:

$$\min_u E_2(u), \quad \text{where } E_2(u) = \int_{\Omega} \left( u_{xx}^2 + u_{xy}^2 + u_{yx}^2 + u_{yy}^2 \right)^{\frac{1}{2}} \, dxdy + \frac{\lambda_2}{2} \int_{\Omega} |u - u_0|^2 \, dxdy, \quad (4)$$

where the parameter  $\lambda_2 > 0$  balances the regularity of the solution and how well  $u$  fits the noisy data  $u_0$ . Minimizing functional (4) yields a nonlinear fourth-order PDE. The details about how to get this nonlinear fourth-order PDE and its boundary conditions were omitted in [6] due to its complexity. In this work, we shall supply these details together with some details about its numerical implementations.

Higher-order PDEs are known to recover smoother surfaces. Dealing with higher-order PDEs a major challenge is to pursue the quality of (1) along jumps.

Unfortunately, it seems to be a hard case to get one method to preserve discontinuities in one part of the image and simultaneously recover smooth signals in other parts. Hence, a combination of different methods may be needed to improve the image restoration capability. Our approach is to involve both a lower- and a higher-order PDE, a solution strategy motivated by [7, 8, 17, 18], among others.

The novelty in this work is to involve the restoration properties of (1) together with (4), i.e. using convex combination of the solutions of (1) and (4). By analyzing underlying features or the local trend in the image of interest, we can combine (1) and (4) in such a way that both smooth and discontinuous signals are handled properly. The ROF [1] model (1) is known to be better than the LLT [6] model (4) when identifying locations of discontinuities and the amplitude of jumps. The LLT model handles smooth signals better than the ROF model. A combined model is able to utilize the best properties of each of the two models, and manage to overcome the weaknesses of both.

Different approaches for adaptive image restoration methods have been considered before [7, 8, 17, 18, 19, 20, 21]. In [7],  $u$  was decomposed into a sum of a smooth function  $u_1$  and a function  $u_2$  that contained the jumps. They solved an inf-convolution problem concerning  $u_1$  and  $u_2$ . The strategy in [8] was to introduce an elliptic operator together with (1). This substantially reduced the staircase effect, while edges were preserved. Further, in [17], functional (1) was modified by the extra term  $\frac{\mu}{2} \int_{\Omega} |\nabla u|^2 dx dy$ ,  $\mu > 0$ . This ensures convexity of the cost functional in  $H_0^1(\Omega)$ , and yields the unique solvability of the problem in this space. Common drawbacks of the adaptive formulations mentioned above, are the increased number of unknown to determine leading to increased computing time. In [18] they employed and generalized the enhancement technique based on BV- and Perona-Malik-type regularization methods. A cost functional consisting of a data fitting term and a restoration energy criterion for objects consisting of edge, flat, and intermediate regions was minimized. Global convergence was proven.

The idea we use here seems to have some similarities with the ideas used in [19, 20, 21]. For example, the following functional is used as a regularization term in [21] in computing a visible-surface representation  $u(x, y)$ ;

$$S_{\rho\tau}(u) = \frac{1}{2} \int_{\Omega} \rho(x, y) \{ \tau(x, y) (u_{xx}^2 + 2u_{xy}^2 + u_{yy}^2) + [1 - \tau(x, y)] (u_x^2 + u_y^2) \} dx dy.$$

The function  $\rho(x, y)$  is chosen to be small at jumps and  $\tau(x, y) \in [0, 1]$  is used to control the regularity of the surface. In our approach,  $\rho$  is not necessary due to the use of the total variational norms and the function of  $\tau$  is replaced by a linear combination technique using a weighting function. The approach using the weighting function could automatically detect jumps and smooth regions. Thus, it has better properties and is easy and cheap to compute.

To deal with the unknown parameters presented in our approach, i.e.  $\lambda_1$  in (1) and  $\lambda_2$  in (4), we assume the noise level

$$\sigma^2 = \int_{\Omega} |u - u_0|^2 dx dy \quad (5)$$

to be approximately known. The minimizers for (1) and (4) can then be combined with (5) to find an optimal value for  $\lambda_1$  and  $\lambda_2$ , respectively. Without this assumption,  $\lambda_1$  and  $\lambda_2$  can be found by trial and error, or by adjusting a parameter  $\bar{\sigma}$  to approximate the true noise level  $\sigma$  in (5). Examples of image restoration with such approximation of the noise level will also be evaluated.

Section 2 of this paper gives a detailed description of minimization problem (4), and we formally introduce the fourth-order PDE appearing in the image restoration model. This fourth-order PDE together with a second-order PDE are the basic ingredients in our composed model. The way these two PDEs interfere with each other is discussed in Section 3. Implementation details are given in Section 4. Section 5 is devoted to numerical examples, followed by some conclusions in Section 6.

## 2 Description of minimization problem (4)

It is in our interest to restore an image that is contaminated with noise. We use functionals  $E_i$ ,  $i = 1, 2$ , to measure the quality of the restoration process. Smaller values of  $E_i$  correspond to a result that reflects features (flat, smooth and jumps) in a better way than larger values do. One of the two basis functionals in our approach is given by (1). From [1] we know that minimizing functional (1) yields the associated Lagrange equation

$$-\nabla \cdot \left( \frac{\nabla u}{|\nabla u|} \right) + \lambda_1(u - u_0) = 0 \quad \text{in } \Omega, \quad \frac{\partial u}{\partial n} = 0 \quad \text{on } \partial\Omega. \quad (6)$$

Further, recall from [1] that the unknown parameter  $\lambda_1$  is given by

$$\lambda_1 = -\frac{1}{\sigma^2} \int_{\Omega} \left( \frac{\nabla u}{|\nabla u|} \right) \cdot \nabla(u - u_0) \, dx dy. \quad (7)$$

An iterative method is used to solve (6) and (7) so that the solution satisfies these equations at steady state, c.f. [1]. We want to find an equivalent formulation for minimization problem (4). For simplicity we introduce the notation  $|D^2u| = \left( \nabla u_x \cdot \nabla u_x + \nabla u_y \cdot \nabla u_y \right)^{\frac{1}{2}} = \left( u_{xx}^2 + u_{xy}^2 + u_{yx}^2 + u_{yy}^2 \right)^{\frac{1}{2}}$  and write

$$E_2(u) = \int_{\Omega} |D^2u| \, dx dy + \frac{\lambda_2}{2} \int_{\Omega} |u - u_0|^2 \, dx dy. \quad (8)$$

To find a weak solution for (8) we must investigate

$$\frac{\partial E}{\partial u} \cdot v = \int_{\Omega} \left( \frac{\nabla u_x \cdot \nabla v_x + \nabla u_y \cdot \nabla v_y}{|D^2u|} \right) \, dx dy + \lambda_2 \int_{\Omega} (u - u_0)v \, dx dy = 0. \quad (9)$$

Using Green's lemma on the first part of (9) we get

$$\begin{aligned} \int_{\Omega} \left( \frac{\nabla u_x \cdot \nabla v_x + \nabla u_y \cdot \nabla v_y}{|D^2 u|} \right) dx dy &= \int_{\partial\Omega} \left( \frac{1}{|D^2 u|} \frac{\partial u_x}{\partial n} \right) v_x + \left( \frac{1}{|D^2 u|} \frac{\partial u_y}{\partial n} \right) v_y dS \\ &\quad - \int_{\Omega} \nabla \cdot \left( \frac{\nabla u_x}{|D^2 u|} \right) v_x + \nabla \cdot \left( \frac{\nabla u_y}{|D^2 u|} \right) v_y dx dy, \end{aligned} \quad (10)$$

where  $dS$  denotes the surface measure on  $\partial\Omega$ . Here and later, the unit normal vector on  $\partial\Omega$  is denoted by  $n = (n_1, n_2)$ . Let us also introduce the notation  $\overline{G} = [g_1, g_2] = \left[ \nabla \cdot \left( \frac{\nabla u_x}{|D^2 u|} \right), \nabla \cdot \left( \frac{\nabla u_y}{|D^2 u|} \right) \right]$ . Applying Green's lemma on the vector field  $\overline{G}$ , we obtain

$$\int_{\Omega} \overline{G} \cdot \nabla v dx dy = \int_{\partial\Omega} \overline{G} \cdot n v dS - \int_{\Omega} \nabla \cdot \overline{G} v dx dy. \quad (11)$$

By combining (10) and (11) together with the notation of  $\overline{G}$ , we see that

$$\begin{aligned} \int_{\Omega} \left( \frac{\nabla u_x \cdot \nabla v_x + \nabla u_y \cdot \nabla v_y}{|D^2 u|} \right) dx dy &= \int_{\partial\Omega} \left( \frac{1}{|D^2 u|} \frac{\partial u_x}{\partial n} \right) v_x + \left( \frac{1}{|D^2 u|} \frac{\partial u_y}{\partial n} \right) v_y dS \\ &\quad - \int_{\partial\Omega} \nabla \cdot \left( \frac{\nabla u_x}{|D^2 u|} \right) n_1 v + \nabla \cdot \left( \frac{\nabla u_y}{|D^2 u|} \right) n_2 v dS \\ &\quad + \int_{\Omega} \left( \nabla \cdot \left( \frac{\nabla u_x}{|D^2 u|} \right) \right)_x v + \left( \nabla \cdot \left( \frac{\nabla u_y}{|D^2 u|} \right) \right)_y v dx dy. \end{aligned} \quad (12)$$

From this we conclude that a minimum for (8) occurs when

$$\left( \frac{u_{xx}}{|D^2 u|} \right)_{xx} + \left( \frac{u_{xy}}{|D^2 u|} \right)_{yx} + \left( \frac{u_{yx}}{|D^2 u|} \right)_{xy} + \left( \frac{u_{yy}}{|D^2 u|} \right)_{yy} + \lambda_2 (u - u_0) = 0. \quad (13)$$

If  $\Omega$  is a rectangular domain, with an outer normal  $n = (n_1, n_2)$ , we see from (12) that the variational equality (9) implies the following the boundary conditions

$$\left. \begin{aligned} u_{xx} + u_{yy} &= 0 \\ \left( \frac{u_{xx}}{|D^2 u|} \right)_x + \left( \frac{u_{xy}}{|D^2 u|} \right)_y &= 0 \end{aligned} \right\} \text{on } \partial\Omega \text{ where } n \text{ is orthogonal to the } y\text{-axe}, \quad (14)$$

$$\left. \begin{aligned} u_{yy} + u_{xx} &= 0 \\ \left( \frac{u_{yx}}{|D^2 u|} \right)_x + \left( \frac{u_{yy}}{|D^2 u|} \right)_y &= 0 \end{aligned} \right\} \text{on } \partial\Omega \text{ where } n \text{ is orthogonal to the } x\text{-axe}. \quad (15)$$

The value of  $\lambda_2$  also needs to be determined such that (13) has a steady state with condition (5) fulfilled at the steady state. We use the same idea as in [1] to obtain such a formula for  $\lambda_2$ . We simply multiply (13) by  $u - u_0$ , integrate over  $\Omega$ , and make use of (5) to get

$$\lambda_2 = \frac{-1}{\sigma^2} \int_{\Omega} \left( \frac{u_{xx}}{|D^2 u|} (u - u_0)_{xx} + \frac{u_{xy}}{|D^2 u|} (u - u_0)_{yx} + \frac{u_{yx}}{|D^2 u|} (u - u_0)_{xy} + \frac{u_{yy}}{|D^2 u|} (u - u_0)_{yy} \right) dx dy. \quad (16)$$

In this section we have treated  $E_1(u)$  and  $E_2(u)$  and their associated Lagrangian equations separately. However, we want to establish a positive interaction between these equations and that is the topic for the next section.

### 3 Convex combination of the two minimization problems

Here, we use the notation  $u$  and  $v$  to distinguish the solutions of (6) and (13) respectively. From the Euler-Lagrange variational principle, the minimizer of  $u$  and the minimizer of  $v$  can be interpreted as the steady state solution of the nonlinear diffusion process

$$u_t = \nabla \cdot \left( \frac{\nabla u}{|\nabla u|} \right) - \lambda_1(u - u_0), \quad \text{and} \quad (17)$$

$$v_t = -\left( \frac{v_{xx}}{|D^2v|} \right)_{xx} - \left( \frac{v_{xy}}{|D^2v|} \right)_{yx} - \left( \frac{v_{yx}}{|D^2v|} \right)_{xy} - \left( \frac{v_{yy}}{|D^2v|} \right)_{yy} - \lambda_2(v - u_0), \quad (18)$$

where we respectively use the initial condition  $u(x, y, 0) = u_0(x, y)$  and  $v(x, y, 0) = u_0(x, y)$ . Each of the above PDEs substantially suppress noise, but we do not expect their solutions  $u$  and  $v$  to be equal all over the image domain  $\Omega$ , mainly because (17) does not penalize discontinuities while (18) is known to recover smoother surfaces. Both methods have their strengths and weaknesses depending on the characteristics of the image of interest. Because of this, we want to generate a new solution by taking the best from each of the two methods by a convex combination  $w = \theta u + (1 - \theta)v$ , for  $\theta \in [0, 1]$ . We prefer that the weighting function  $\theta$  can be found adaptively. Due to the strengths and weaknesses of the two models, it is desirable that the weighting function  $\theta = 1$  along edges and in flat regions, emphasizing the restoration properties for (17). To emphasize the restoration properties for (18) in smooth regions we want  $0 \leq \theta < 1$ . By testing several different approaches calculating the weighting function, we have found the procedure to update  $\theta$  discussed below is rather stable and gives good results.

Assume that we have a weighting function  $\theta^{old}$ , a function  $u$  which is an intermediate solution of (17) and a function  $v$  which is an intermediate solution of (18). We shall find a new weighting function  $\theta^{new}$  according to

$$\theta^{new} = \begin{cases} 1 & \text{if } |\nabla w| \geq c \\ \frac{1}{2} \cos\left(\frac{2\pi|\nabla w|}{c}\right) + \frac{1}{2} & \text{elsewhere,} \end{cases} \quad (19)$$

where  $w = \theta^{old}u + (1 - \theta^{old})v$ . We define this mapping from  $u, v, \theta^{old}$  to  $\theta^{new}$  as  $\psi$ , i.e.  $\theta^{new} = \psi(\theta^{old}, u, v)$ . For large and small values of  $|\nabla w|$  the weight  $\theta$  approaches 1, and for intermediate values of  $|\nabla w|$  the weight function is closer to 0. The positive parameter  $c$  must be adjusted so that  $\theta$  reaches its minimum value

in regions that are linearly sloped. A typical example of the relationship between  $|\nabla w|$ ,  $c$  and  $\theta$  are given in Figure 1.

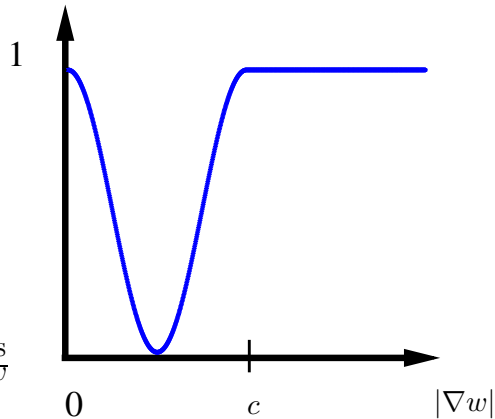


Figure 1: An example of the weight function  $\theta$  given by (19).

Choosing  $0 \ll c < 1$  means that only the absolute largest jumps are unaffected of the fourth-order PDE (18). Since only small jumps (staircase effect) caused by (17) should be suppressed with fourth-order PDE (18) we found  $c \in (\frac{1}{20}, \frac{1}{5})$  to be a proper value if  $|\nabla w|$  is scaled to take values in the interval  $[0, 1]$ . With this choice of  $c$  intermediate jumps were protected while the staircase effect was suppressed, but this parameter is image dependent.

## 4 Implementation details

To discretize the equations (17) and (18), we use finite differences. Let  $\Delta x$  and  $\Delta y$  be the mesh sizes for the  $x$  and  $y$  variables, and  $\Delta t$  be the time step. We denote by  $u^k$  and  $v^k$  the approximations for  $u(x, y, k\Delta t)$  and  $v(x, y, k\Delta t)$  respectively, where  $x$  and  $y$  are the grid points. The approximations we have used in our scheme is outlined in Table 1.

Table 1: Discretization used in the implementations.

$D_x^\pm(u_{i,j})$	$\pm \frac{1}{\Delta x} [u_{i\pm 1,j} - u_{i,j}]$
$D_y^\pm(u_{i,j})$	$\pm \frac{1}{\Delta y} [u_{i,j\pm 1} - u_{i,j}]$
$D_{xx}(u_{i,j})$	$\frac{1}{\Delta x} [D_x^+(u_{i,j}) - D_x^+(u_{i-1,j})]$
$D_{xy}^\pm(u_{i,j})$	$\pm \frac{1}{\Delta y} [D_x^\pm(u_{i,j\pm 1}) - D_x^\pm(u_{i,j})]$
$D_{yx}^\pm(u_{i,j})$	$\pm \frac{1}{\Delta x} [D_y^\pm(u_{i\pm 1,j}) - D_y^\pm(u_{i,j})]$
$D_{yy}(u_{i,j})$	$\frac{1}{\Delta y} [D_y^+(u_{i,j}) - D_y^+(u_{i,j-1})]$
$ D_x(u_{i,j}) $	$\sqrt{(D_x^+(u_{i,j}))^2 + (m[D_y^+(u_{i,j}), D_y^-(u_{i,j})])^2 + \epsilon}$
$ D_y(u_{i,j}) $	$\sqrt{(m[D_x^+(u_{i,j}), D_x^-(u_{i,j})])^2 + (D_y^+(u_{i,j}))^2 + \epsilon}$
$ D^2(u_{i,j}) $	$\sqrt{(D_{xx}(u_{i,j}))^2 + (D_{xy}^+(u_{i,j}))^2 + (D_{yx}^+(u_{i,j}))^2 + (D_{yy}(u_{i,j}))^2 + \epsilon}$

To simplify the notations, we will omit the subscripts  $i, j$  and use  $u^k$  to denote  $u_{i,j}^k$ . In Table 1 we have used the notation  $m[a, b] = \left(\frac{\text{sign } a + \text{sign } b}{2}\right) \min(|a|, |b|)$ . The details of the algorithm we have used are given in the following.

**Algorithm 1** Given  $\theta^0 \in [0, 1]$ ,  $c \in [0, 1]$  and put  $u^0 = v^0 = u_0$ . For  $k = 0, 1, \dots$ , do

1. Find  $\lambda_1^k$  by (7) and update

$$\tilde{u}^{k+1} = u^k + \Delta t D_x^- \left( \frac{D_x^+ u^k}{|D_x u^k|} \right) + \Delta t D_y^- \left( \frac{D_y^+ u^k}{|D_y u^k|} \right) - \Delta t \lambda_1^k (u^k - u_0). \quad (20)$$

2. Find  $\lambda_2^k$  by (16) and update

$$\begin{aligned} \tilde{v}^{k+1} = v^k - \Delta t \left[ D_{xx} \left( \frac{D_{xx} v^k}{|D^2 v^k|} \right) + D_{yx}^- \left( \frac{D_{xy}^+ v^k}{|D^2 v^k|} \right) \right. \\ \left. + D_{xy}^+ \left( \frac{D_{yx}^- v^k}{|D^2 v^k|} \right) + D_{yy} \left( \frac{D_{yy} v^k}{|D^2 v^k|} \right) \right] - \Delta t \lambda_2^k (v^k - u_0). \end{aligned} \quad (21)$$

3. Find  $\theta^{k+1}$  from (19), i.e.

$$\theta^{k+1} = \psi(\theta^k, \tilde{u}^{k+1}, \tilde{v}^{k+1}).$$

4. Do the convex combination

$$u^{k+1} = \theta^{k+1} \tilde{u}^{k+1} + (1 - \theta^{k+1}) \tilde{v}^{k+1}, \quad \text{and let } v^{k+1} = u^{k+1}.$$

When evaluating the finite differences for (20) and (21), the boundary conditions (6) and (14)-(15) are needed. Implementation of (6) is explained in [1], and implementation of (14)-(15) follows from Table 1.

Notice that a convex combination is done in each iteration for this algorithm. Another approach could be to find the solution  $u$  and  $v$  independent of each other, and combine them at convergence. Numerical tests indicate that a combination in each iteration is most effective and accurate. Each of the numerical schemes (20) and (21) are stable if they are solved separately, as long as  $\Delta t$  fulfills the Courant-Friedrichs-Lewy (or CFL) stability criterion. Numerical tests have shown that the same holds if we combine them in each iteration. Moreover, the time step needed by the combined scheme Algorithm 1 is always larger than in the fourth-order scheme; the combined scheme not only improves the quality of the processed image; it also improves the efficiency compared with the fourth-order scheme.

## 5 Numerical results

In this section we present some of the results obtained with the proposed Iterative Image Restoration (IIR) model by alternating between PDE (17) and PDE (18). Our results will be compared with the standard ROF model [1] given by solving PDE (17), and the LLT model [6] given by solving PDE (18). For the numerical examples we will use images composed of flat subregions, subregions with a smooth change in the intensity value, and jumps. We expect ROF to restore and enhance jumps more precisely than LLT does. On the other hand, we expect LLT to process smooth subregions more correctly than ROF does. See [6] for a closer evaluation of ROF and LLT. Using IIR the aim is to take the best out of each of these methods to recover both jumps and smooth signals accurately.

In Figure 2, two gray-level images are depicted, together with the corresponding intensity plots. At first glance, one may mistakenly think that the bright region in the central part of the image in Figure 2(a) takes a constant intensity value, but the intensity plot in Figure 2(c) reveals that there is a smooth change in the intensity value in this region. To emphasize these details it is therefore essential to visualize the results with both intensity plots and contour plots when we compare the performance for the different schemes. To do a thorough evaluation, we will also investigate and report the signal-to-noise-ratio (SNR) and the  $L_2$ -norm of the difference between the recovered image and the true image. For a given image  $u$  and its noise observation  $u_0$ , the noise is denoted as  $\eta = u_0 - u$ . The following formula has been used to calculate the SNR for the numerical experiments for a given image  $u$  and noise  $\eta$ ;

$$\text{SNR} = \frac{\int_{\Omega} (u_0 - \bar{u}_0)^2 dx dy}{\int_{\Omega} (\eta - \bar{\eta})^2 dx dy}, \quad \text{where } \bar{u}_0 = \frac{1}{|\Omega|} \int_{\Omega} u_0 dx dy, \quad \text{and } \bar{\eta} = \frac{1}{|\Omega|} \int_{\Omega} \eta dx dy.$$

In our first example, we used the noisy data shown in Figure 2(b) as input to the ROF, LLT and IIR. Before processing, we observed  $\|u_0 - u_{true}\|_{L^2}^2 \approx 1.88 \cdot$

$10^5$  and  $\text{SNR} \approx 12$ . There are several reasons for examine the image shown in Figure 2(a). First of all, it consists of a rotationally invariant object, i.e. circular edges. Secondly, evaluating an object like this should provoke the strengths and the weaknesses for the three restoration methods listed above.

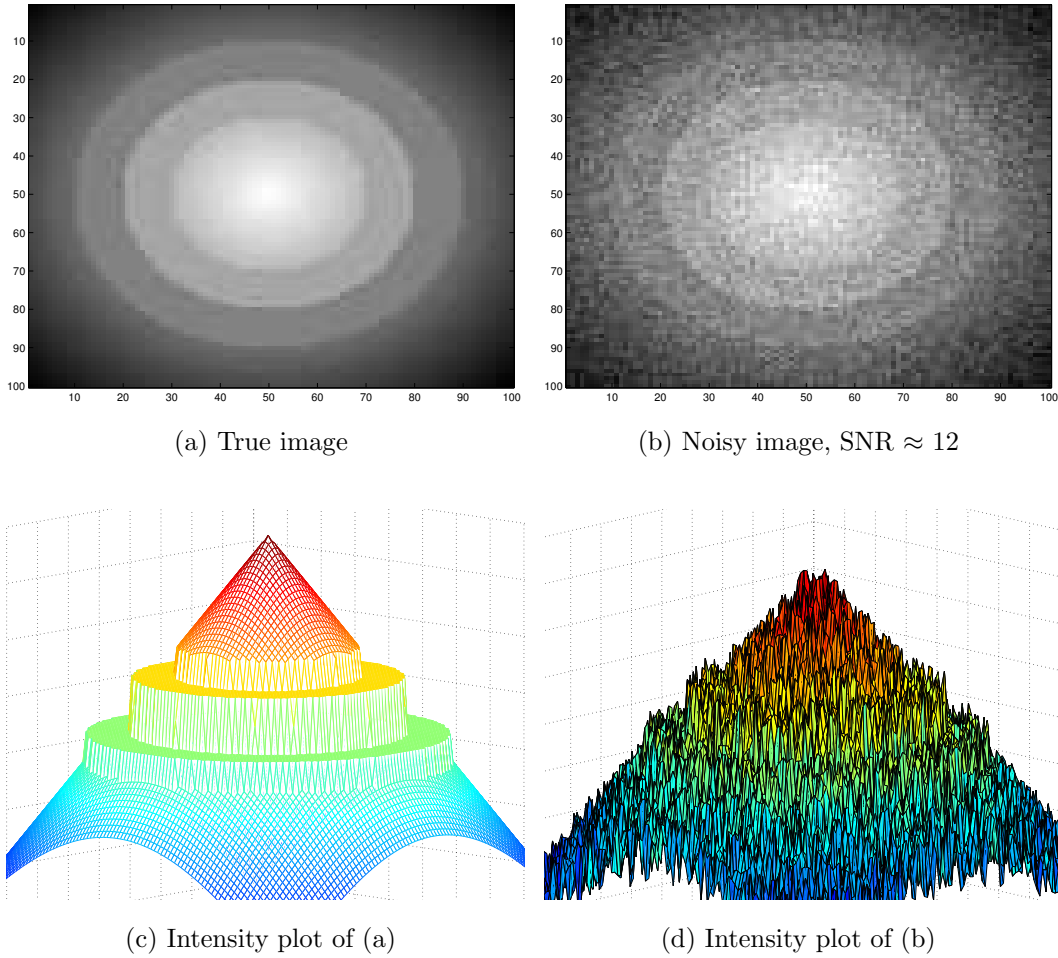
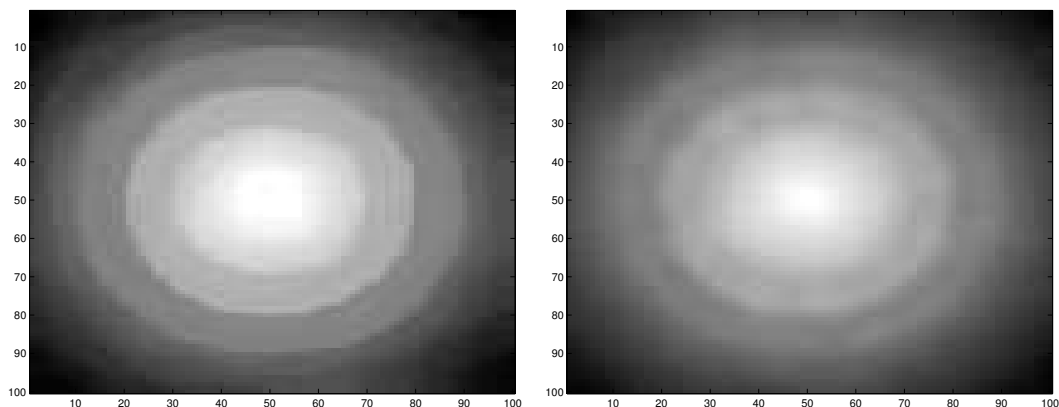


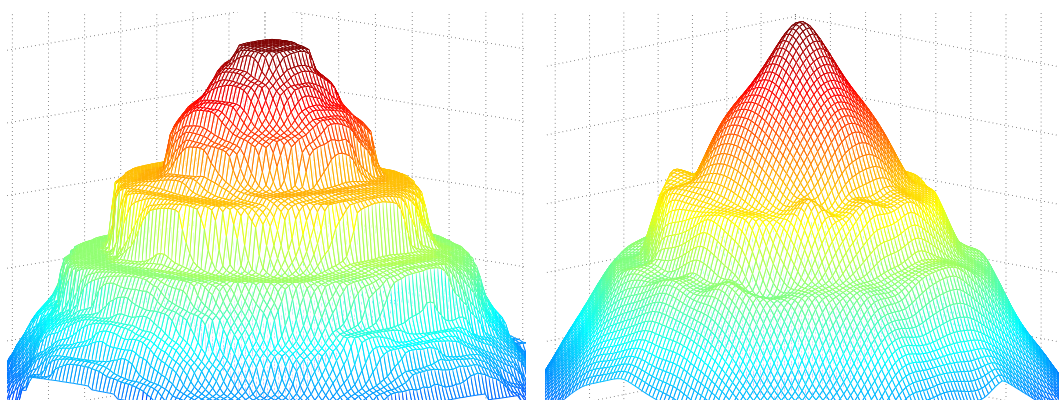
Figure 2: Two different ways to visualize the same data are given in the upper and lower column. Regions with high function values in the lower column correspond to bright regions in the images at the upper column.

In this first test we were specially interested in evaluating (i) the ability to reproduce the cone on the top of the object, (ii) the ability to maintain the height of the object, (iii) the ability to reproduce jumps and flat regions, and (iv) the spurious staircase effect in smooth regions.



(a) Processed with ROF

(b) Processed with LLT



(c) Intensity plot of (a)

(d) Intensity plot of (b)

Figure 3: Two different approaches are used to find an improved image from the noisy image given in Figure 2(b). Only the central portion of the intensity plots is depicted in the lower column.

Let us first focus on the result obtained with ROF depicted in Figure 3(a) and (c). The smooth change in the intensity value (i.e. the cone) is recovered as piecewise constant subregions, as seen in Figure 3(c). This is a known byproduct of the TV-norm methods in image restoration. On the other hand, flat regions and all edges in this image are recovered accurately by ROF. Concerning the result obtained with LLT, we observe that the staircase effect in smooth regions is suppressed but edges are not recovered that accurately with this model. By comparing Figure 3(c)-(d) with Figure 2(c), the strengths and the weaknesses of the restoration schemes ROF and LLT are clearly visible.

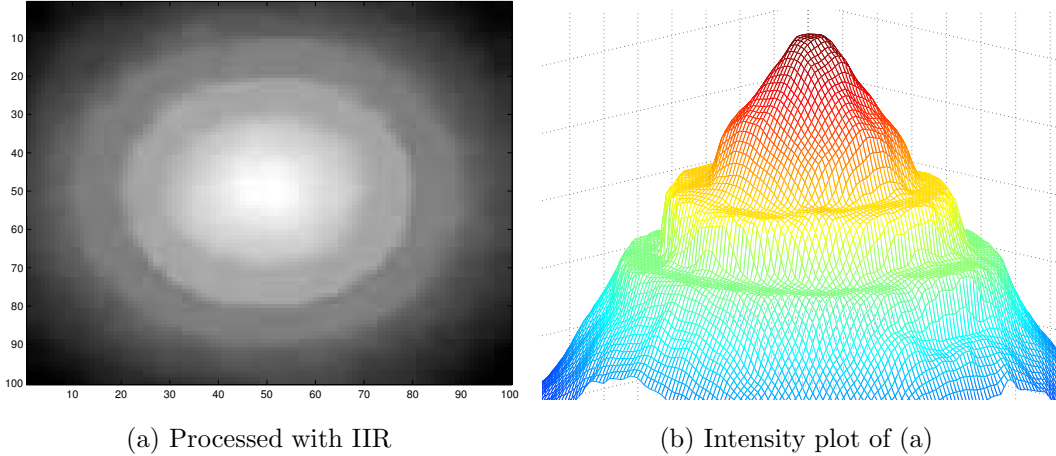


Figure 4: IIR is used to find an improved image from the noisy image given in Figure 2(b). Only the central portion of the intensity plot is depicted here.

All edges are recovered accurately with the iterative model as seen in Figure 4. At the same time, the staircase effect in smooth regions is avoided. These are important improvements. Also when we evaluated the SNR and the  $L^2$ -norm some progress was found in the result achieved with the IIR model.

Table 2: SNR,  $L^2$ -norm and  $\Delta t_{max}$  for the different schemes.

Method	SNR	$L^2$ -norm	$\Delta t_{max}$ (CFL)
ROF	115	$1.64 \cdot 10^4$	0.35
LLT	148	$1.66 \cdot 10^4$	0.09
IIR	163	$1.22 \cdot 10^4$	0.17

From Table 2 we see that the  $L^2$ -norm is reduced approximately 11.5 times by both ROF and LLT, and 15.5 times by using the IIR model. These numbers indicate that some progress is made with IIR, but the important issues are that IIR recovers smoother sub-surfaces where ROF suffers from the staircase effect and simultaneously preserves discontinuities in other parts of the image. We observed that choosing  $\Delta t > \Delta t_{max}$  made the schemes unstable. The ratio between the three CFL-conditions is representative for what we found in other tests. Higher-order PDEs are known to have more restricted time step than lower-order PDEs. One important observation is that the time step restriction  $\Delta t_{max}$  for IIR is not bounded by the time step restriction for LLT, although the LLT model is incorporated in the IIR model.

For the convex combination  $\theta u + (1 - \theta)v$  in IIR, it is essential that the contributions from  $v$  are suppressed at major discontinuities. The weight function  $\theta$  given by (19) controls the interplay between  $u$  from (17) and  $v$  from (18) in IIR. In Figure 5 we visualize  $\theta$  at convergence. This gray-level image indicates the ratio between (17) and (18) for IIR. It is interesting to observe that all flat regions are marked as bright regions, i.e.  $\theta \approx 1$ , meaning that no contribution from  $v$  occurs in this region. For regions where smooth sub surfaces should be restored we find  $\theta < 1$ . This indicates that  $\theta$  is estimated in accordance with the image features given in Figure 2(c).

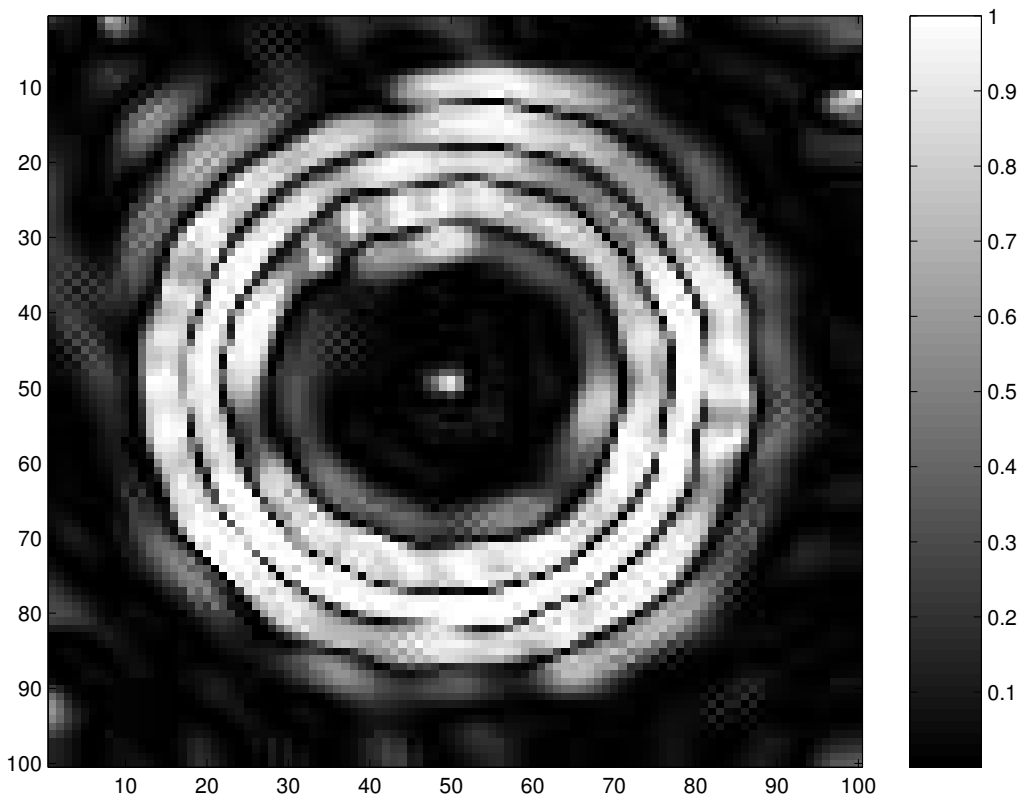


Figure 5: Weight function  $\theta$  at convergence.

In the next example the Lena image was corrupted with Gaussian distributed noise. Before processing  $\text{SNR} \approx 10$  and  $L^2$ -norm  $\approx 1.97 \cdot 10^7$ . In real applications the exact noise level is seldom known. To simulate such a case the value we use for  $\sigma$  in (7) and (16) is not the true noise level, but an approximation of the true noise level  $\bar{\sigma}$ . Let  $\sigma$  denote the noise level we use for the algorithms and  $\bar{\sigma}$  denote the true noise level. For the Lena image given in Figure 6(b) we challenge the schemes by a poor estimate for the amount of noise when we deal with the noise constraint,  $\sigma^2 = \frac{10}{14}\bar{\sigma}^2$ .

Table 3: SNR,  $L^2$ -norm and  $\Delta t_{max}$  for the different schemes.

Method	SNR	$L^2$ -norm	$\Delta t_{max}$ (CFL)
ROF	35	$4.79 \cdot 10^6$	1.10
LLT	40	$4.26 \cdot 10^6$	0.24
IIR	43	$4.05 \cdot 10^6$	0.80

Both ROF, LLT and IIR improve the restoration capacity when the correct estimate for the amount of noise is used for the noise level constraint, but these results are not reported here. As in Table 2, we observe some progress using IIR compared with the two other schemes. However, the important issue is whether IIR recovers smoother sub surfaces where ROF suffers from the staircase effect, and simultaneously preserves discontinuities in other parts, also for natural images. We zoom in the two regions marked with white rectangles in Figure 6(c) for a more definite evaluation of the processed images.

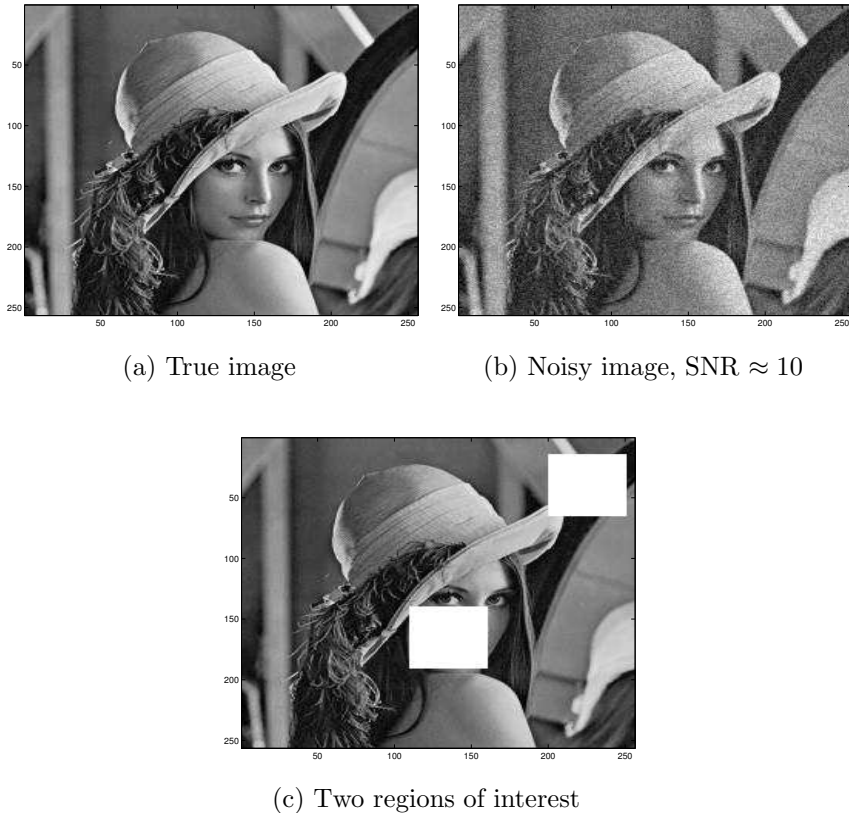
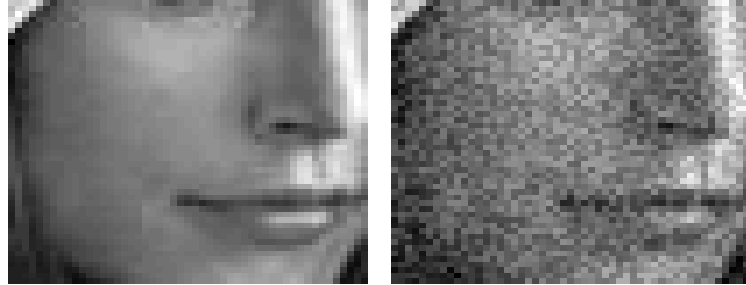


Figure 6: Lena image corrupted with Gaussian distributed noise. The white rectangles in (c) indicate two regions of special interest, i.e. one typical smooth region and one region with discontinuities.



(a) True image

(b) Noisy image, SNR  $\approx 10$



(c) Processed with ROF

(d) Processed with LLT

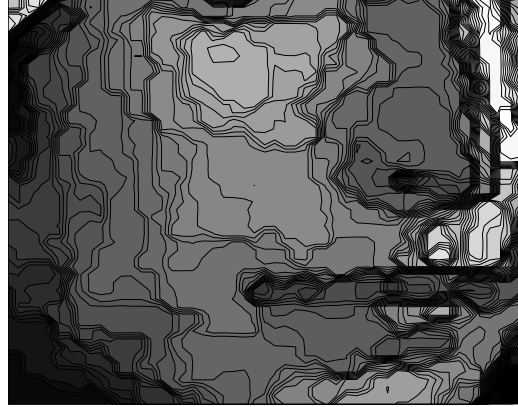
(e) Processed with IIR

Figure 7: A small portion of the Lena image is shown to better emphasize disparities in the smooth surface.

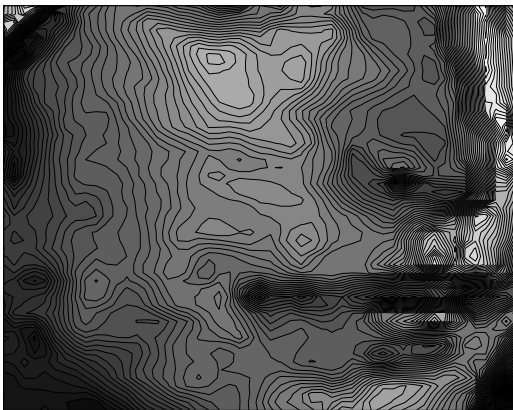
A small portion of the Lena image is shown in Figure 7. As expected, ROF transforms smooth subregions like the cheek into piecewise constant regions. Both LLT and IIR restore images with smoother surfaces that match Figure 7(a) in a better way. It is not easy to distinguish between the two images depicted in Figure 7(d) and (e). In this part of the image the weight function  $\theta$ , given in Figure 10, emphasize the effect of (18) in the convex combination between (17) and (18) for IIR, and therefore the results from LLT and IIR are similar in this part of the image. This effect is even better visualized in a contour plot given in Figure 8. From the contours, we see that the results produced by LLT and IIR is much smoother than the result of ROF and they also match the true contours in a better way. All the three methods are able to preserve the discontinuity around the lips and nose.



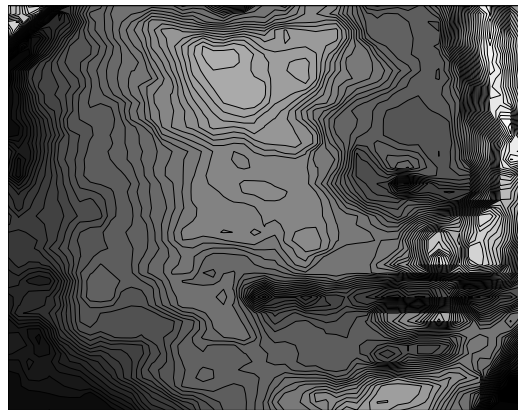
(a) Ideal contour plot



(b) Result with ROF



(c) Result with LLT



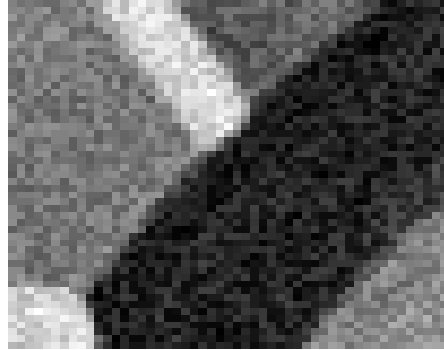
(d) Result with IIR

Figure 8: A small portion of the Lena image is visualized with a contour plot to better emphasize disparities between the models.

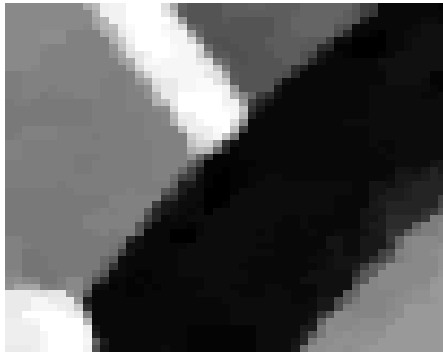
Next, we want to evaluate the performance of the three different methods in regions that are dominated by discontinuities and piecewise constant signals, see Figure 9. In regions with edges we observe that ROF restores and enhances these image features in a better way than LLT, see Figure 9(c) and (d). Both ROF and IIR recover images with edges in accordance with Figure 9(a). It is not easy to distinguish between the two images depicted in Figure 9(c) and (e). Along the discontinuities the weight function  $\theta$ , given in Figure 10, emphasizes the effect of (17) in the convex combination between (17) and (18) for IIR, therefore the results from ROF and IIR are similar in this part of the image.



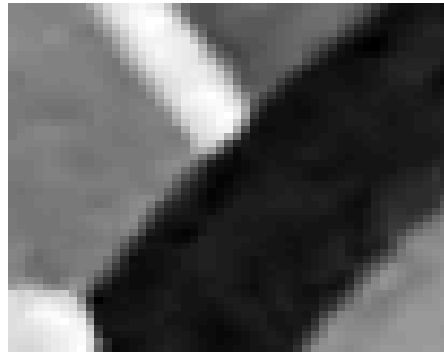
(a) True image



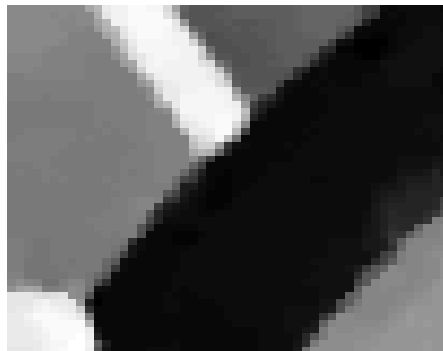
(b) Noisy image, SNR  $\approx 10$



(c) Processed with ROF



(d) Processed with LLT



(e) Processed with IIR

Figure 9: A part of the Lena image with discontinuities.

The weight function  $\theta$  given by (19) at convergence is shown in Figure 10. The gray-level indicates the ratio between (17) and (18) for IIR. It is interesting to

observe that all major edges are marked as bright regions, i.e.  $\theta = 1$ , meaning that IIR automatically preserves image boundaries in these regions while suppressing noise.

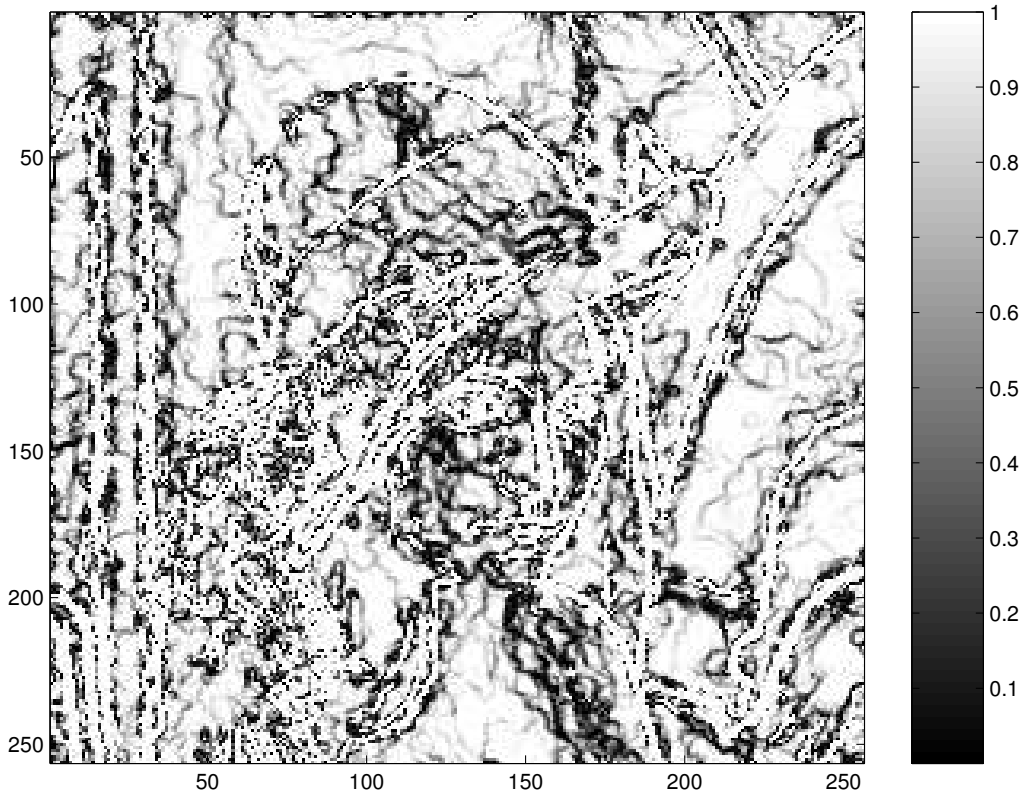


Figure 10: Weight function  $\theta$  at convergence.

## 6 Conclusions

This paper describes a method for filtering gray-scale images corrupted by i.i.d. Gaussian noise. The proposed method combines the TV-norm filter of Rudin, Osher and Fatemi (ROF) in [1] with a fourth-order PDE filter of Lysaker, Lundervold and Tai (LLT) in [6]. The algorithm, which we call an "Iterative Image Restoration" (IIR) model, is based on a convex combination of the two corresponding solutions of ROF and LLT, and an iterative way to determine the weighted average of these two solutions. We have tested the IIR algorithm on images consisting of edge, flat and smooth sub-regions. The proposed algorithm is able to locate discontinuities as accurate as the ROF algorithm, and, at the same time do a better job in regions with a smooth variation. Moreover, the combined algorithm is able to use a much less restrictive CFL condition than the fourth-order scheme of

LLT. This is confirmed by numerical experiments. Due to the complexity of the equations involved, it is not easy to supply a theoretical verification for this.

## References

- [1] L.I. Rudin, S. Osher, and E. Fatemi, “Nonlinear total variation based noise removal algorithms,” *Physica D*, vol. 60, pp. 259–268, 1992.
- [2] William P. Ziemer, *Weakly differentiable functions*, vol. 120 of *Graduate Texts in Mathematics*, Springer-Verlag, New York, 1989, Sobolev spaces and functions of bounded variation.
- [3] Giusti E, *Minimal Surface and Functions of Bounded Variations*, Boston, Birkhäuser, 1998.
- [4] Weickert J., *Anisotropic Diffusion in Image Processing*, Stuttgart, B. G. Teubner, 1998.
- [5] W. Ring, “Structural properties of solutions to total variation regularization problems,” *M2AN Mathematical Modeling and Numerical analyses*, vol. 34, no. 4, pp. 799–810, 2000.
- [6] M. Lysaker, A. Lundervold, and X.-C. Tai, “Noise Removal Using Fourth-Order Partial Differential Equation with Applications to Medical Magnetic Resonance Images in Space and Time,” *IEEE Trans. Image Processing*, vol. 12, no. 12, pp. 1579–1590, 2003.
- [7] A. Chambolle and P-L. Lions, “Image recovery via total variation minimization and related problems,” *Numerische Mathematik*, vol. 76, pp. 167–188, 1997.
- [8] T. Chan, A. Marquina, and P. Mulet, “High-Order Total Variation-Based Image Restoration,” *SIAM Journal on Scientific Computation*, vol. 22, pp. 503–516, 2000.
- [9] Y.-L. You and M. Kaveh, “Fourth-Order Partial Differential Equation for Noise Removal,” *IEEE Transactions on Image Processing*, vol. 9, no. 10, pp. 1723–1730, 2000.
- [10] M. Lysaker, S. Osher, and X.-C. Tai, “Noise Removal Using Smoothed Normals and Surface Fitting,” *IEEE Trans. Image Processing*, vol. 13, no. 10, pp. 1345–1357, 2004.
- [11] S. Osher, A. Sole, and L. Vese, “Image decomposition and restoration using total variation minimization and the  $H^{-1}$  norm,” *Multiscale Modeling and Simulation: A SIAM Interdisciplinary Journal*, vol. 1, no. 3, pp. 349–370, 2003.

- [12] J. B. Greer and A. L. Bertozzi, “ $H^1$  Solutions of a Class of Fourth Order Non-linear Equations for Image Processing,” *Discrete and continuous dynamical systems 2004, special issue in honor of Mark Vishik*, Editors: V. Chepyzhov, M. Efendiev, Alain Miranville, and Roger Temam, vol. 1-2, no. 10, pp. 349–366, 2004.
- [13] J. B. Greer and A. L. Bertozzi, “Traveling Wave Solutions of Fourth Order PDEs for Image Processing,” Tech. rep. (03-25), UCLA, Applied mathematics, 2003.
- [14] A. L. Bertozzi and J. B. Greer, “Low Curvature Image Simplifiers: Global Regularity of Smooth Solutions and Laplacian Limiting Schemes,” Tech. rep. (03-26), UCLA, Applied mathematics, 2003.
- [15] O. Scherzer, “Denoising with higher order derivatives of bounded variation and an application to parameter estimation,” *Computing*, vol. 60, pp. 1–27, 1998.
- [16] W. Hinterberger and O. Scherzer, “Variational methods on the space of functions of bounded Hessian for convexification and denoising,” *Preprint*, 2004.
- [17] T. Karkkainen and K. Majava, “SAC-methods for Image Restoration,” *World Scientific and Engineering Society, Greece*, pp. 162–167, 2000.
- [18] K. Ito and K. Kunisch, “BV-type regularization methods for convoluted objects with edge, flat and grey scales,” *Inverse Problems*, vol. 16, pp. 909–928, 2000.
- [19] M. Nagao and T. Matsuyama, “Edge preserving smoothing, computer graphics and image processing,” *Computer Graphics and Image Processing*, vol. 9, no. 4, pp. 394–407, 1979.
- [20] D. Terzopoulos, “Regularization of inverse visual problems involving discontinuities,” *IEEE Transactions on Pattern Analysis and Machine Intelligence*, vol. 8, no. 4, pp. 413–424, 1986.
- [21] D. Terzopoulos, “The computation of visible-surface representations,” *IEEE Trans Pattern Anal Mach Intell*, vol. 10, no. 4, pp. 417–438, 1988.